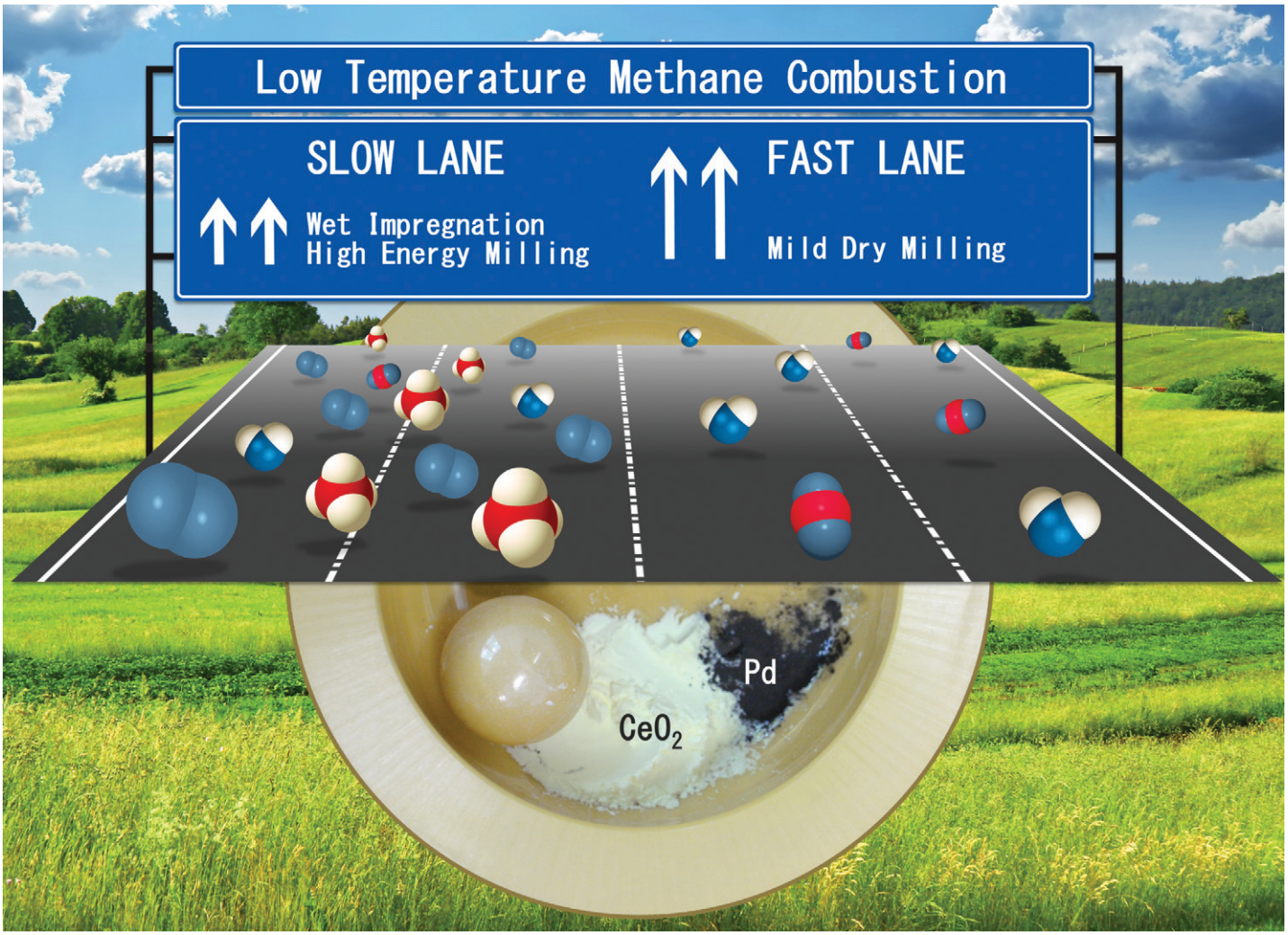

Showcasing research from a joint study between University of Udine-Catalysis Lab and Technical University of Catalonia-Barcelona Tech.

The effect of milling parameters on the mechanochemical synthesis of Pd–CeO_2 methane oxidation catalysts

The correlation among milling parameters, nanoscale morphology and CH_4 oxidation activity was explored, showing that samples prepared by a dry milling process under mild conditions are able to fully convert methane at lower temperatures compared to samples obtained by conventional impregnation or high-energy milling. Image by M. Danielis.

As featured in:

See Sara Colussi *et al.*, *Catal. Sci. Technol.*, 2019, **9**, 4232.

ROYAL SOCIETY OF CHEMISTRY | Celebrating IYPT 2019

rsc.li/catalysis

Registered charity number: 207890

Catalysis Science & Technology

PAPER

View Article Online
View Journal | View Issue

Cite this: *Catal. Sci. Technol.*, 2019, **9**, 4232

The effect of milling parameters on the mechanochemical synthesis of Pd–CeO_2 methane oxidation catalysts†

Maila Danielis, [a] Sara Colussi, *[a] Carla de Leitenburg, [a] Lluís Soler, [b] Jordi Llorca [b] and Alessandro Trovarelli [a]

Received 4th June 2019,
Accepted 9th July 2019

DOI: 10.1039/c9cy01098j

rsc.li/catalysis

The preparation of catalytic materials *via* mechanochemical routes is a very promising alternative to complex wet chemical syntheses due to its simplicity, versatility and ecological advantages. The mechanical mixing of Pd nanoparticles and CeO_2 results in very active methane oxidation catalysts; here we explore the effect of milling parameters on the overall performance of Pd–ceria catalysts. The high methane combustion activity is the result of nanoscale interaction between palladium and cerium oxide and it is shown to be strongly dependent on the intensity of milling. This was investigated through methane combustion tests up to 1173 K and characterized by means of temperature programmed oxidation and reduction experiments. The morphological features of the obtained materials were investigated by HRTEM analysis and correlated to the catalytic behavior.

Introduction

The discovery of untapped natural gas deposits and the possible valorization of waste through biogas production have prompted the development of new technologies for natural gas utilization, among which its use as fuel for transportation or for distributed small-scale power generation. This in turn has focused the attention on the possible dangers of methane leaks into the atmosphere, since CH_4 is a strong greenhouse gas, and consequently on methane abatement. Due to the intrinsic unreactive nature of the CH_4 molecule, the oxidation of methane has always represented a challenge, and numerous studies have been published.[1–5] Nevertheless, its increasing application to natural gas fueled vehicles emission control,[3] reduction of secondary pollutants from controlled natural gas combustion[6] and methane activation for the production of feedstock molecules[7,8] is continuously pushing towards the development of catalytic systems with increased activity and stability.

Palladium is known as one of the most active metals for methane activation, and CeO_2 addition proved to lead to a synergetic effect on Pd-based catalysts.[9–12] In particular, ionic Pd species in strong interaction with ceria are reported both theoretically[13–15] and experimentally[16] as extremely active for methane combustion, enabling activation also by the hydrogen abstraction route.[17] In addition, this configuration appears able to hinder the steam deactivation, as reported recently by our group.[18] Water vapor in fact is known as a strong inhibitor for methane combustion[19–21] and it represents an especially important issue for automotive aftertreatment applications, since exhaust gases contain around 10–15 vol% of water vapor produced by fuel combustion in the engine chamber.

Among the variety of chemical synthesis approaches, mechano-chemistry is the oldest known method for the preparation of materials, as the very simple act of mixing different compounds together to transform them into a new product was already experienced in the prehistoric times.[22,23] Fast forward to the modern times, the mechano-chemical route for the synthesis of products or for promoting chemical reaction (even in gas-phase)[24] has been developed mostly in the material science field. Mechanical energy enables the creation of metastable structures bypassing the thermodynamic and chemical equilibria and it is of particular interest for the synthesis of new alloys or nanocomposite materials.[25–27] In the latest decades, the advances in mechano-chemical technology have spread to other fields such as catalysis, where it has been successfully applied to the synthesis of advanced nanomaterials for electrochemical applications,[28,29] mixed oxides,[30,31] metallorganic materials[32] and many others.[33–36] Nevertheless, its wide range of variable parameters and the combination of mechanical and chemical effects has hindered the straightforward application to oxide-supported

[a] *Dipartimento Politecnico, Università di Udine, and INSTM, via del Cotonificio 108, 33200 Udine, Italy. E-mail: sara.colussi@uniud.it*
[b] *Institute of Energy Technologies, Department of Chemical Engineering and Barcelona Research Center in Multiscale Science and Engineering, Universitat Politècnica de Catalunya, EEBE, Eduard Maristany 10-14, 08019 Barcelona, Spain*
† Electronic supplementary information (ESI) available. See DOI: 10.1039/c9cy01098j

metal catalysts.[37,38] Often an experimental trial-and-error approach is needed to find the best synthesis conditions, depending on the choice of the precursors and on the desired applications.[39] In general, high energies are employed in order to induce interaction and alloying at nanoscale.

We recently reported an extremely active methane oxidation Pd–CeO_2 catalyst prepared by a mild milling process.[40] The low intensity milling brought to the creation of an amorphous Pd–Ce layer covering the ceria crystallites, where the enhanced nanoscale interaction was at the origin of an outstanding methane oxidation activity. Here, we investigate the effect of milling conditions on this catalytic system in order to further study the resulting Pd–CeO_2 interaction. Starting from metallic palladium and cerium oxide powders, we varied the milling time and energy and analyzed their effect on the morphological features and the methane oxidation activity.

Experimental

Catalyst preparation

All catalysts considered in this work contain 1 wt% Pd and were prepared using Pd black (Sigma Aldrich, BET surface area 40 $m^2\ g^{-1}$) as palladium precursor and pure CeO_2 calcined at 1173 K as support oxide (Treibacher Industrie, BET surface area 3 $m^2\ g^{-1}$). The preparation of Pd/CeO_2 was carried out by mixing of the powders under different milling conditions. The reference PdCeM sample was synthesized in a Pulverisette 23 Minimill by milling Pd and ceria powders for 10 minutes at 15 Hz in a 15 ml zirconia jar using one zirconia ball (15 mm diameter, 10 g, ball-to-powder ratio = 10).[40] For comparison, other Pd–ceria formulations were prepared by mixing the two components with lower or higher intensity with respect to PdCeM. Low intensity mixing was achieved when palladium nanoparticles and ceria powders were loosely mixed inside the jar in the absence of grinding balls (denoted as PdCeL) or simply grinded in an agate mortar for 10 minutes (PdCeG). On the medium-high intensity side, one sample was prepared by milling for 1 hour in the same conditions as PdCeM (Pulverisette 23 Minimill, 15 Hz and one zirconia ball, named PdCeM 1 h), while other samples were prepared in a Spex8000 Mixer Mill rotating at 875 rpm in a 50 ml jar with 9 zirconia balls (10 mm diameter, total BPR = 20) for milling times ranging from 5 minutes to 8 hours. These last samples are referred to as PdCeHM (high-intensity milling).

Characterization and testing

The materials were characterized by means of BET surface area measurements, XRD analysis, ICP elemental analysis for Pd content, Raman spectroscopy and HRTEM. BET surface area measurements were carried out in a Micrometrics Tristar Porosimeter analyzing N_2 adsorption isotherms at 77 K. XRD analysis was performed in a Philips X'Pert diffractrometer equipped with an X'Celerator detector using Ni-filtered Cu Kα radiation (λ = 1.542 Å) recording spectra in the 20–100° 2θ range (0.02° step size, 40 s counting time per step). Microstructural characterization by high-resolution transmission electron microscopy was carried out at 200 kV with a JEOL JEM-2010F electron microscope equipped with a field emission gun. Raman spectra were collected with an Xplora Plus Micro-Raman system (Horiba), exciting the samples with a 532 nm radiation. Spectra were collected at room temperature with a resolution of 1 cm^{-1} and 2 accumulations of 10 s with a 50× LWD objective.

Methane combustion tests were carried out under a slightly lean atmosphere (0.5% CH_4, 2% O_2, balance He, 180 ml min^{-1}) by heating the sample up to 1173 K for two heating/cooling cycles. To investigate the palladium oxidation–decomposition and reduction behavior, temperature programmed oxidation (TPO) and reduction (TPR) tests were performed under oxygen (2% O_2 in N_2, 60 ml min^{-1}) and hydrogen (4.5% H_2 in N_2, 35 ml min^{-1}) feed, respectively. In oxidation tests 150 mg of sample are heated up to 1273 K and cooled to RT at 10 K min^{-1} for three consecutive heating/cooling cycles; the oxygen concentration is monitored with an on-line ABB AO2020 Magnos 106 paramagnetic analyzer. TPR tests are carried out in a Micromeritics Autochem II 2920 analyzer on 50 mg of sample loaded in a U-shaped quartz reactor. The catalyst is pretreated in air at 623 K for 1 hour, cooled by pumping liquid N_2 down to 193 K and then heated from 193 K to 1223 K at 10 K min^{-1} under hydrogen.

Reaction rates were measured in differential conditions after a first light-off cycle at 623 K (Table 1) and the verification of kinetic regime is reported in the ESI.†

Results and discussion

Table 1 and Fig. S1† show respectively BET surface area and powder X-ray diffraction profiles of all the samples investigated. The mixing of ceria and Pd at low intensity (PdCeL and PdCeG) results in samples having a surface area in the range 2–4 $m^2\ g^{-1}$, similar to the initial support surface area. Also with PdCeM textural properties are not affected, while an increase of surface area to 5 $m^2\ g^{-1}$ is observed in the sample milled at low intensity for 1 h. Milling at a higher energy causes a significant increase of surface area, which is typically observed in high-energy milling of powders.[27] This is due to continuous fragmentation of particles during milling with consequent reduction of crystallite size down to a few nanometers, as can be measured from peak enlargement in the X-ray diffraction profiles of high-energy milled powders (Table 1). X-ray diffraction profiles for all samples show peaks belonging to main reflections of CeO_2 fluorite phase. In one sample only (PdCeHM8h) a slight shift of the diffraction profile at higher angles indicates formation of solid solution between CeO_2 and ZrO_2 originating from the milling media. The high energy impact and friction that characterize milling in this sample can explain the leaching of ZrO_2 from the balls and jar with insertion of Zr inside CeO_2 lattice, as already observed under similar milling conditions.[31,41] For the same reason diffraction peaks belonging to free ZrO_2 are

Table 1 Characterization and activity data of samples prepared in this study

Sample[a]	Pd loading (wt%)	BET surface area ($m^2\ g^{-1}$)	Crystallite size[b] (nm)	Reaction rate ($\mu mol\ g_{Pd}^{-1}\ s^{-1}$)
CeO_2	—	2.6	47.2	—
PdCeL	1[c]	2.9	47.1	35.7[e]
PdCeG	0.8[d]	3.2	47.1	205[f]
PdCeM	0.8[d]	3.5	47.0	208[f]
PdCeM 1 h	0.82[d]	5.0	42.1	206[f]
PdCeHM 5 min	0.87[d]	11.6	28.9	52.6[e]
PdCeHM 30 min	1[c]	23.1	12.3	11.6[e]
PdCeHM 1 h	1[c]	23.7	11.6	9.1[e]
PdCeHM 8 h	1[c]	25.6	9.5	0.8[e]

[a] L (loosely mixed in a Pulverisette Minimill without grinding balls), G (mixed in an agate mortar for 10 minutes), M (mixed in a Pulverisette Minimill at 15 Hz using one 15 mm diameter zirconia ball and a ball/powder ratio of 10), HM (mixed in a Spex8000 Mixer Mill rotating at 875 rpm with nine 10 mm diameter zirconia balls and a ball/powder ratio of 20). [b] Estimated using Scherrer equation.[42] [c] Nominal loading. [d] Measured by ICP. [e] Measured at 623 K in a flow reactor under 5% conversion. [f] Calculated under differential conditions in a recycle reactor at 623 K.

also detected. Weak XRD signals due to Pd are also distinguished in the fresh samples (see inset of Fig. S1†).

In Fig. 1 the light-off curves of combustion tests measured under the same conditions are reported for all prepared samples. The heating and cooling ramps are shown separately and refer to the second combustion cycle, where the catalytic behavior is usually stabilized.[40] To better compare the activity, in Fig. 2 are reported the temperatures at which 10% CH_4 conversion was achieved (T_{10}) during combustion tests. Fig. 2 shows also reaction rates measured at 623 K for all samples as reported in Table 1. As it can be observed there is a narrow window of optimal milling conditions which result in highly active Pd/CeO_2 catalyst.

These conditions depend heavily on the characteristics of the milling and on the milling time. Mild grinding in an agate mortar (PdCeG) or milling in a Minimill (PdCeM milled at 15 Hz with one single grinding ball) for up to 1 h led to the lowest ignition temperatures, as seen by the light-off curves in Fig. 1 and the corresponding T_{10} reported in Fig. 2. Conversely, milling in the high energy Spex8000 mill brought to very different results. While the overall rpm and BPR were similar to the P23 Minimill conditions (*i.e.* 900 rpm and BPR = 10), the increased amount of grinding balls brought to an exponential increase of ball-to-ball impacts.[43] Since the milling spheres possess high kinetic energy, the impacts among them confer a much higher energy to the milled powders compared to ball-to-wall impacts, as the jar walls have kinetic energy equal to zero.[44] As a consequence, in the Spex8000

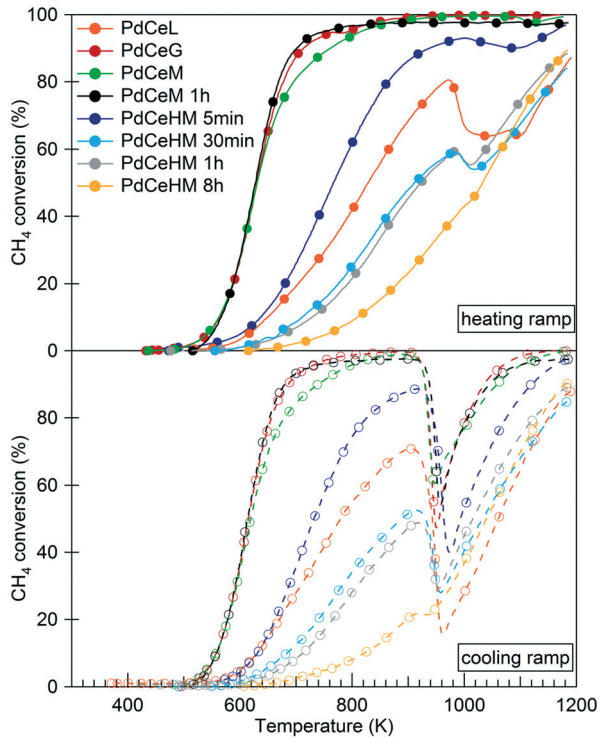

Fig. 1 Methane oxidation tests; second combustion cycle. Solid line: heating; dashed line: cooling.

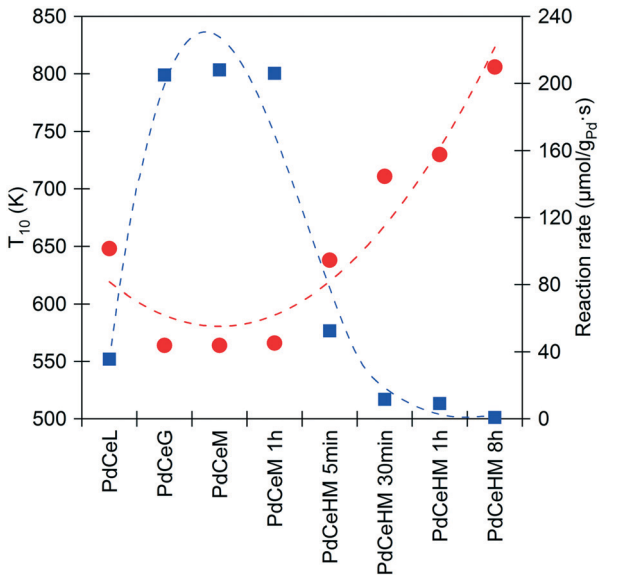

Fig. 2 Temperatures of 10% methane conversion in the second TPC cycle (red circles) and reaction rates measured at 623 K (blue squares).

mill the powders are subjected to more frequent and energetic collisions, while in the Minimill arrangement and in the agate mortar mostly shear stresses are developed due to the friction of the single ball or the pestle on the walls.

At nanoscale, this may influence the fracture–relaxation phenomena occurring at the interface[22] with a strong effect on the properties of the catalytic materials obtained. In fact, as evidenced by data in Fig. 2 and the light-off curves in Fig. 1, the HM samples display poor methane oxidation activity which further decreases with prolonged milling times. It can also be observed from Table 1 that these impacts are able to break down the particles with a decrease in crystallite size and a consequent increase of surface area. In addition, at longer milling time, impacts can partially transfer zirconium ions from the milling media to the powder, thus leading to a contamination of the support. Both phenomena are typically observed when milling powders under similar conditions.[28,31]

The different interaction developed between ceria and palladium was further characterized by temperature programmed oxidation (TPO) tests and HRTEM investigation. Fig. 3 shows TPO profiles of the most representative samples in the first two heating/cooling cycles. Further TPO cycles do not modify the overall profile and the second TPO is therefore indicative of the behavior of the sample under catalytic conditions. PdCeM profile shows a broad oxygen uptake in the first cycle during heating between 450 K and 750 K. This is common to all samples investigated, excluding PdCeHM8h, and it is due to the complete oxidation of the metallic Pd nanoparticles to PdO as quantitatively shown in Table 2 with an oxygen uptake ranging from 6.3 to 7.7 mmoles O_2 per g that is close to the oxidation of *ca.* 100% of metallic Pd to PdO (uptake 0 in Table 2). At *ca.* 1040 K the decomposition of PdO to Pd takes place in one single peak (release 1). During cooling reformation of PdO occurs at lower temperature (*ca.* 910 K, uptake 1) showing the typical hysteresis of Pd/PdO formation/decomposition.[45] In the second cycle, decomposition of PdO to Pd occurs in three successive steps (release 2) suggesting the presence of strongly interacting Pd–Ce–O species which decompose at high temperatures (1120 K) and that are usually related to a high methane oxidation activity.[46] Reformation of PdO during cooling (uptake 2) is qualitatively and quantitatively similar to PdO formation in the first cycle (uptake 1). In all cases the quantity of oxygen uptaken or released correspond to the oxidation or decomposition of *ca.* 100% of Pd/PdO. In PdCeL quantitative low temperature oxidation of Pd to PdO and high temperature decomposition of PdO to Pd is observed, with the latter occurring at slightly lower temperature than in PdCeM. However, only *ca.* 10% of loaded Pd is able to undergo oxidation during cooling, while in the following second cycle Pd has substantially lost its cycling capabilities.

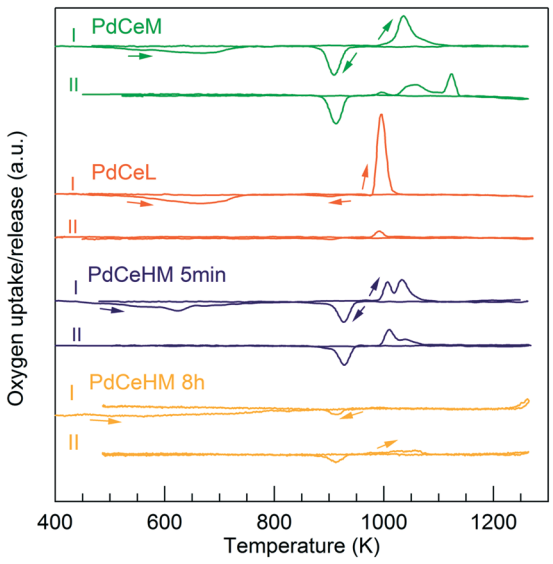

Fig. 3 Oxygen uptake and release profiles, first and second TPO cycle.

This is likely due to the insufficient contact established between the metal and the support during loose mixing which causes most of the Pd not in contact with ceria to sinter at high temperature and become inactive. This explains the lower activity of PdCeL shown in Fig. 1; on this sample the interaction between palladium and ceria is weak and during the first heating cycle at temperatures higher than 970 K, PdO decomposes to Pd metal (see Fig. S2 in the ESI†), likely followed by the sintering of metal particles. During cooling their increased size prevents re-oxidation, thus losing active sites for the subsequent combustion cycles. Indeed, XRD measurements after reaction reveal the presence of highly crystalline metallic Pd (see Fig. S1†). Likely, the absence of the grinding ball hinders the creation of surface defects[47] or highly reactive sites[48] on the ceria surface, hence providing few anchoring sites for insertion and spreading of Pd. It is interesting, though, that even this very gentle mixing of Pd and ceria provides some interaction between the two components, as the catalytic behavior of PdCeL is better than that of bare Pd nanoparticles loosely mixed with quartz (Fig. S3†), where the activity heavily dropped at *ca.* 1173 K and does not recover in subsequent cycles.

On the samples milled at higher energy a progressive decrease in the amount of cycling Pd can be observed. On the PdCeHM 5 min sample two distinct palladium oxide decomposition peaks appear in the first heating ramp, accounting for only 75% of all loaded Pd. During cooling, around 50% of the loaded metal is re-oxidized, which again decomposes in the second heating ramp in two steps between 1010 K and 1040 K. These peaks are usually attributed in the literature to superficial and bulk palladium oxide.[46] On the sample milled for 8 hours a negligible decomposition peak can be observed at 1000 K. During cooling, the characteristic O_2 absorption peak for Pd re-oxidation appears at slightly lower temperatures compared to other ceria-supported samples due to the inclusion of zirconium ions from the milling media in the ceria lattice.[10] The quantitative analysis of the oxygen uptake and release in the second heating/cooling cycle indicates that only *ca.* 20% of all loaded Pd participates in the decomposition/re-oxidation cycle.

Table 2 Quantitative analysis of TPO profiles

	I cycle			II cycle	
Sample name	Uptake 0 (μmoles O_2 per g)	Release 1 (μmoles O_2 per g)	Uptake 1 (μmoles O_2 per g)	Release 2 (μmoles O_2 per g)	Uptake 2 (μmoles O_2 per g)
PdCeM	6.28 (110)[a]	5.61 (99)	5.01 (89)	5.43 (96)	5.11 (91)
PdCeL	6.63 (94)	6.53 (93)	0.96 (13)	1.01 (14)	0.67 (9)
PdCe HM 5 min	7.73 (126)	4.58 (75)	3.13 (51)	2.82 (46)	3.12 (51)
PdCe HM 8 h	—	0.03 (0)	1.12 (16)	1.50 (21)	1.72 (24)

[a] The amount of Pd (% of total Pd) that is involved in oxidation/decomposition is reported in parentheses.

HRTEM characterization allows us to observe in more detail the morphological characteristics of Pd–ceria catalysts as a function of milling parameters. When the contact energy is too low, Pd aggregates appear in weak contact with ceria, as shown in Fig. 4(A and B). On the other hand, when Pd and CeO_2 are subject to soft milling and mostly shear stresses, the characteristic amorphous layer with embedded Pd is observed,[40] both in PdCeM and PdCeG samples (Fig. 4(C) and (D), respectively). Under hard milling conditions, *i.e.* with a higher number of grinding balls, the palladium particles appear well defined and partially embedded inside the ceria lattice. On the PdCeHM 5 min sample large Pd particles can be observed either in a flattened form (Fig. 4(E)) or strongly anchored to the support crystal lattice (Fig. 4(F)). It is possible that part of these particles are so strongly embedded inside the ceria lattice that, once oxidized in the first heating ramp in combustion or oxidation tests, they are not reactive anymore and do not participate in the typical PdO–Pd–PdO hysteresis behavior at high temperature. The remaining part, in weaker contact with ceria, is likely the one contributing to the oxygen uptake and release shown in Fig. 3 and responsible for the relatively poor catalytic activity observed. Prolonged milling times, as in the PdCeHM 8 h sample, lead to the insertion of these palladium particles inside the support.

Fig. 4(G and H) illustrate profile views of the sample where PdO particles are present and covered by a ceria layer. These HRTEM images suggest that the high mechanical energy developed is not only able to break ceria crystallites in smaller ones, as seen by the high surface area of this sample, but also to oxidize Pd particles to PdO which remains entrapped within ceria. The enclosed palladium is therefore not available for methane oxidation, which is in agreement with the progressive loss of activity with increasing milling times observed in light-off curves (Fig. 1 and 2).

Interestingly, after exposure of this sample under oxidizing conditions at high temperatures (1273 K), HRTEM observations evidence that part of the palladium oxide is disclosed and becomes exposed on the ceria surface. Indeed, the resulting PdO particles can be seen by HRTEM images in Fig. 5(A and B): they lack any encapsulation and are characterized by a relatively large average dimension (around 10 nm). Some smaller features can also be observed on the ceria surface (Fig. 5(C)), likely attributed to other palladium oxide species but too small for further HRTEM analysis. The newly exposed palladium is poorly active towards methane

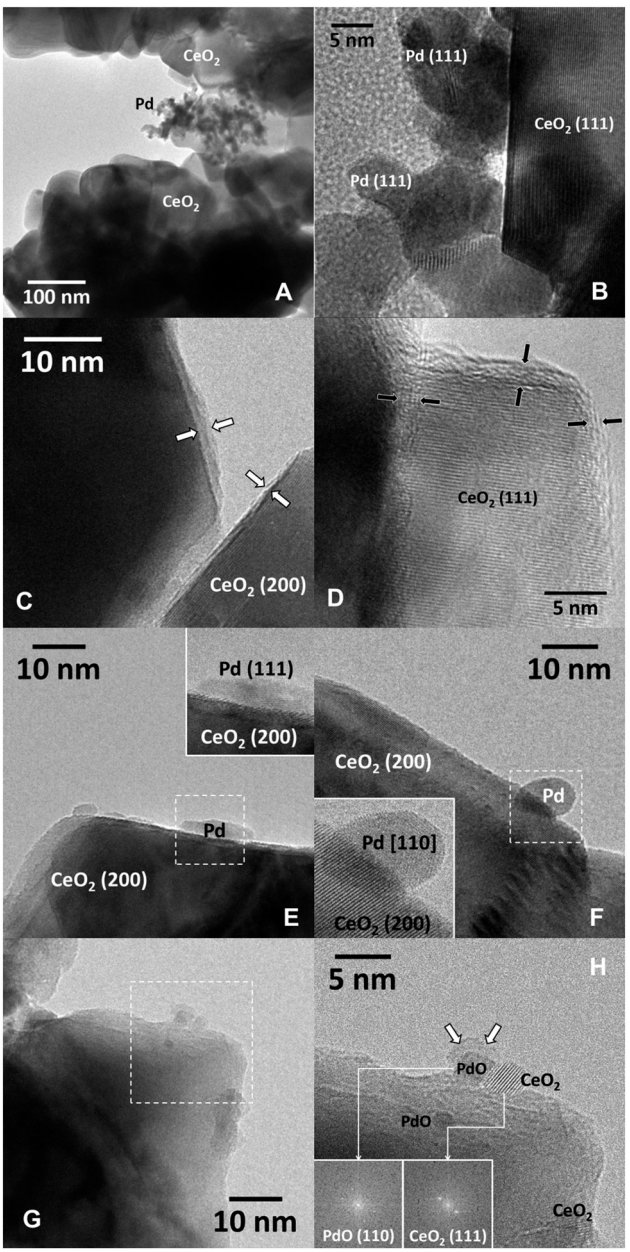

Fig. 4 HRTEM images of (A and B) PdCeL, (C) PdCeM, (D) PdCeG, (E and F) PdCeHM 5 min, (G and H) PdCeHM 8 h.

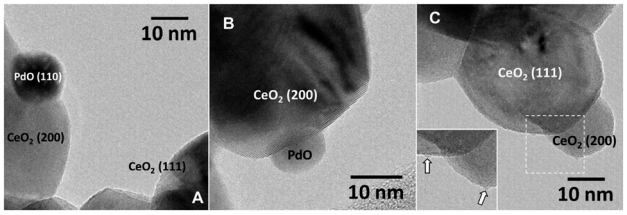

Fig. 5 HRTEM images of PdCeHM 8 h after oxidation test performed up to 1273 K, exhibiting large PdO particles (A and B) and smaller features (C) on the ceria surface.

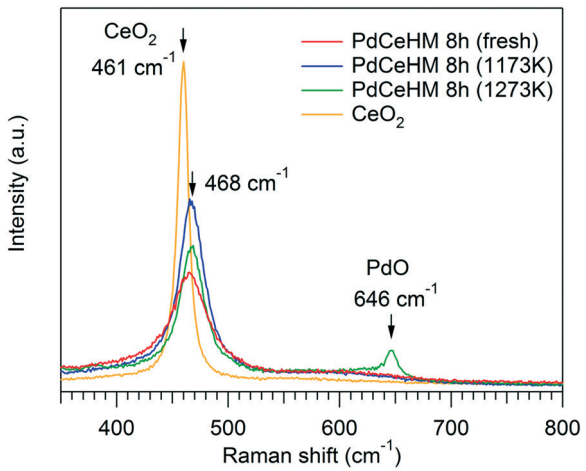

Fig. 6 Raman spectra collected on PdCeHM 8 h fresh, after combustion test at 1173 K and after oxidation test at 1273 K.

oxidation, as seen in Fig. S4† that compares the light-off behavior of PdCeHM 8 h before and after treatment at 1273 K. The lack of activity recovery might be due to the fact that not all the encapsulated palladium segregates to the surface after the thermal treatment, and/or to the low activity of bulk PdO in the low temperature region.[4,40]

The encapsulation of PdO during high energy milling followed by its extraction when treated at high temperatures can be also followed by Raman spectroscopy. The spectra collected on PdCeHM 8 h as prepared and after combustion (1173 K) and oxidation tests (1273 K) are illustrated in Fig. 6. On the fresh milled sample the characteristic PdO peak at around 650 cm^{-1} is absent, and the same profile is obtained on the PdCeHM 8 h sample after combustion reaction up to 1173 K. It is possible that under these conditions the signal of the small PdO entities embedded inside the ceria particles, observed by HRTEM in Fig. 4(G and H), is too attenuated and therefore escapes detection. On the other hand, by thermally treating the sample at 1273 K these palladium species are oxidized and conglomerate in large PdO particles; as a result, the peak at 646 cm^{-1} corresponding to the B_{1g} vibrational mode of PdO is clearly observed. On all samples, the F_{2g} mode of CeO_2 is shifted to 468 cm^{-1}, compared to 461 cm^{-1} observed in fresh ceria, likely due to physical stresses on the ceria surface induced by the high intensity milling process.[49]

Conclusions

The milling of Pd and CeO_2 results in catalytic materials with very different performance in methane combustion. A correlation between the intensity of contact and the properties at nanoscale of Pd and CeO_2 is observed. To prepare active materials an appropriate shear energy must be developed during milling which ensures the embedding and dissolution of metallic Pd particles in an amorphous Pd–ceria layer covering the ceria crystallites.[40] When the energy is insufficient, the palladium particles aggregate in grape-like clusters and display a very low interaction with the support oxide, producing catalysts which initial good activity but leading to a strong activity deterioration during reaction. On the other hand, highly energetic direct impacts flatten and embed large oxidized Pd particles inside of the ceria lattice, making them unavailable for methane activation. High temperature treatment partially reverses this process, with only a limited recovery of activity.

The obtained results differ from the general trends reported in the literature, where usually a high energy is needed in order to induce atomic interactions. Possibly, the peculiar affinity between palladium and ceria combined with their physico-chemical properties ensures that soft shear-like stresses, as those obtained simply grinding in an agate mortar, are enough to have superficial alloying of the two phases in an amorphous layer surrounding the support, which is the key factor for the stabilization of a high methane oxidation activity observed on these materials.

Conflicts of interest

There are no conflicts to declare.

Acknowledgements

Financial support from Ford Motor Company under 2014-2195R URP Award "Three-way catalyst materials for compressed natural gas vehicles" is kindly acknowledged. M. D. acknowledges Regione Friuli Venezia Giulia for funding PhD under Operating Program of the European Social Fund 2014/2020. J. L. is a Sierra Hunter Fellow and is grateful to ICREA Academia program and projects MICINN/FEDER RTI2018-093996-B-C31 and GC 2017 SGR 128.

Notes and references

1 M. Monai, T. Montini, R. J. Gorte and P. Fornasiero, *Eur. J. Inorg. Chem.*, 2018, **25**, 2884–2893.
2 A. Satsuma, K. Osaki, M. Yanagihara, J. Ohyama and K. Shimizu, *Catal. Today*, 2015, **258**, 83–89.
3 R. J. Farrauto, *Science*, 2012, **337**, 659–660.
4 D. Ciuparu, M. R. Lyubovsky, E. Altman, L. D. Pfefferle and A. Datye, *Catal. Rev.: Sci. Eng.*, 2002, **44**, 593–649.
5 J. Lampert, M. Kazi and R. Farrauto, *Appl. Catal., B*, 1997, **14**, 211–223.
6 M. A. Nemitallah, S. S. Rashwan, I. B. Mansir, A. A. Abdelhafez and M. A. Habib, *Energy Fuels*, 2018, **32**, 979–1004.

7 B. Wang, S. Albarracín-Suazo, Y. Pagán-Torres and E. Nikolla, *Catal. Today*, 2017, **285**, 147–158.
8 E. V. Kondratenko, T. Peppel, D. Seeburg, V. A. Kondratenko, N. Kalevaru, A. Martin and S. Wohlrab, *Catal. Sci. Technol.*, 2017, **7**, 366–381.
9 S. Fouladvand, S. Schernich, J. Libuda, H. Grönbeck, T. Pingel, E. Olsson, M. Skoglundh and P.-A. Carlsson, *Top. Catal.*, 2013, **56**, 410–415.
10 S. Colussi, A. Trovarelli, C. Cristiani, L. Lietti and G. Groppi, *Catal. Today*, 2012, **180**, 124–130.
11 M. Cargnello, J. J. D. Jaen, J. C. H. Garrido, K. Bakhmutsky, T. Montini, J. J. C. Gamez, R. J. Gorte and P. Fornasiero, *Science*, 2012, **337**, 713–717.
12 G. Groppi, C. Cristiani, L. Lietti, C. Ramella, M. Valentini and P. Forzatti, *Catal. Today*, 1999, **50**, 399–412.
13 Y.-Q. Su, I. A. W. Filot, J.-X. Liu and E. J. M. Hensen, *ACS Catal.*, 2018, **8**, 75–80.
14 T. P. Senftle, A. C. T. van Duin and M. J. Janik, *ACS Catal.*, 2017, **7**, 327–332.
15 A. D. Mayernick and M. J. Janik, *J. Catal.*, 2011, **278**, 16–25.
16 S. Colussi, A. Gayen, M. Farnesi Camellone, M. Boaro, J. Llorca, S. Fabris and A. Trovarelli, *Angew. Chem., Int. Ed.*, 2009, **48**, 8481–8484.
17 T. P. Senftle, A. C. T. van Duin and M. J. Janik, *ACS Catal.*, 2015, **5**, 6187–6199.
18 A. Toso, S. Colussi, S. Padigapaty, C. de Leitenburg and A. Trovarelli, *Appl. Catal., B*, 2018, **230**, 237–245.
19 R. Gholami, M. Alyani and K. Smith, *Catalysts*, 2015, **5**, 561–594.
20 W. R. Schwartz, D. Ciuparu and L. D. Pfefferle, *J. Phys. Chem. C*, 2012, **116**, 8587–8593.
21 K. Persson, L. D. Pfefferle, W. Schwartz, A. Ersson and S. G. Järås, *Appl. Catal., B*, 2007, **74**, 242–250.
22 P. Baláž, M. Achimovičová, M. Baláž, P. Billik, Z. Cherkezova-Zheleva, J. M. Criado, F. Delogu, E. Dutková, E. Gaffet, F. J. Gotor, R. Kumar, I. Mitov, T. Rojac, M. Senna, A. Streletskii and K. Wieczorek-Ciurowa, *Chem. Soc. Rev.*, 2013, **42**, 7571.
23 L. Takacs, *Chem. Soc. Rev.*, 2013, **42**, 7649.
24 C. Bolm and J. G. Hernández, *Angew. Chem., Int. Ed.*, 2019, **58**, 3285–3299.
25 M. H. Enayati and F. A. Mohamed, *Int. Mater. Rev.*, 2014, **59**, 394–416.
26 V. Šepelák, A. Düvel, M. Wilkening, K.-D. Becker and P. Heitjans, *Chem. Soc. Rev.*, 2013, **42**, 7507.
27 V. Šepelák, S. Bégin-Colin and G. Le Caër, *Dalton Trans.*, 2012, **41**, 11927.
28 T. Kawaguchi, H. Nakamura and S. Watano, *Powder Technol.*, 2017, **305**, 241–249.
29 B. Zhao, Y. Tong, Y. Zhao, T. Yang, F. Yang, Q. Hu and C. Zhao, *Ceram. Int.*, 2015, **41**, 9686–9691.
30 M. H. Enayati, *KONA Powder Part. J.*, 2015, **32**, 196–206.
31 A. Trovarelli, F. Zamar, J. Llorca, C. de Leitenburg, G. Dolcetti and J. T. Kiss, *J. Catal.*, 1997, **169**, 490–502.
32 K. Ralphs, C. Zhang and S. L. James, *Green Chem.*, 2017, **19**, 102–105.
33 M. J. Muñoz-Batista, D. Rodriguez-Padron, A. R. Puente-Santiago and R. Luque, *ACS Sustainable Chem. Eng.*, 2018, **6**, 9530–9544.
34 J.-L. Do and T. Friščić, *ACS Cent. Sci.*, 2017, **3**, 13–19.
35 C. Xu, S. De, A. M. Balu, M. Ojeda and R. Luque, *Chem. Commun.*, 2015, **51**, 6698–6713.
36 K. Ralphs, C. Hardacre and S. L. James, *Chem. Soc. Rev.*, 2013, **42**, 7701.
37 Z. R. Ismagilov, S. V. Kuntsevich, N. V. Shikina, V. V. Kuznetsov, M. A. Kerzhentsev, V. A. Ushakov, V. A. Rogov, A. I. Boronin and V. I. Zaikovsky, *Catal. Today*, 2010, **157**, 217–222.
38 T. Kawabata, H. Matsuoka, T. Shishido, D. Li, Y. Tian, T. Sano and K. Takehira, *Appl. Catal., A*, 2006, **308**, 82–90.
39 Y. Lin, K. A. Watson, M. J. Fallbach, S. Ghose, J. G. Smith, D. M. Delozier, W. Cao, R. E. Crooks and J. W. Connell, *ACS Nano*, 2009, **3**, 871–884.
40 M. Danielis, S. Colussi, C. de Leitenburg, L. Soler, J. Llorca and A. Trovarelli, *Angew. Chem., Int. Ed.*, 2018, **57**, 10212–10216.
41 E. Aneggi, V. Rico-Perez, C. de Leitenburg, S. Maschio, L. Soler, J. Llorca and A. Trovarelli, *Angew. Chem., Int. Ed.*, 2015, **54**, 14040–14043.
42 R. Jenkins and R. L. Snyder, *Introduction to X-ray powder diffractometry*, Wiley, New York, 1996.
43 R. M. Davis, B. McDermott and C. C. Koch, *Metall. Trans. A*, 1988, **19**, 2867–2874.
44 X. Jiang, M. A. Trunov, M. Schoenitz, R. N. Dave and E. L. Dreizin, *J. Alloys Compd.*, 2009, **478**, 246–251.
45 R. J. Farrauto, J. K. Lampert, M. C. Hobson and E. M. Waterman, *Appl. Catal., B*, 1995, **6**, 263–270.
46 S. Colussi, A. Trovarelli, E. Vesselli, A. Baraldi, G. Comelli, G. Groppi and J. Llorca, *Appl. Catal., A*, 2010, **390**, 1–10.
47 Y. Yang, S. Zhang, S. Wang, K. Zhang, H. Wang, J. Huang, S. Deng, B. Wang, Y. Wang and G. Yu, *Environ. Sci. Technol.*, 2015, **49**, 4473–4480.
48 T. X. T. Sayle, M. Cantoni, U. M. Bhatta, S. C. Parker, S. R. Hall, G. Möbus, M. Molinari, D. Reid, S. Seal and D. C. Sayle, *Chem. Mater.*, 2012, **24**, 1811–1821.
49 H. Li, P. Zhang, G. Li, J. Lu, Q. Wu and Y. Gu, *J. Alloys Compd.*, 2016, **682**, 132–137.

